Effect of aberration on height calibration in three-dimensional localization-based microscopy and particle tracking

Yi Deng and Joshua W. Shaevitz*

Department of Physics, Lewis-Sigler Institute for Integrative Genomics, Princeton University, 150 Carl Icahn Laboratory, Princeton, New Jersey 08544, USA

*Corresponding author: shaevitz@princeton.edu

Received 27 October 2008; revised 3 February 2009; accepted 13 February 2009; posted 10 March 2009 (Doc. ID 102840); published 25 March 2009

Many single-particle tracking and localization-based superresolution imaging techniques use the width of a single lateral fluorescence image to estimate a molecule's axial position. This determination is often done by use of a calibration data set derived from a source adhered to a glass–water interface. However, for sources deeper in solution, aberrations will change the relationship between the image width and the axial position. We analyzed the depth-varying point spread function of a high numerical aperture objective near an index of refraction mismatch at the water–glass interface using an optical trap. In addition to the well-known focal shift, spherical aberrations cause up to 30% relative systematic error in axial position estimation. This effect is nonuniform in depth, and we find that, although molecules below the focal plane are correctly localized, molecules deeper than the focal plane are found to be lower than their actual positions. © 2009 Optical Society of America

OCIS codes: 150.1488, 100.2960, 100.6640, 180.0180, 180.2520, 180.6900.

1. Introduction

Over the past several decades, improvements in the resolution of conventional microscopes have led to numerous breakthroughs in the field of molecular and cellular biology. One such advance has been the push toward high-resolution, three-dimensional (3-D) imaging. These techniques include physical rejection of out-of-focus light with a pinhole, termed confocal microscopy [1], using nonlinearities in the photophysics of fluorescent molecules in two-photon and stimulated emission depletion microscopy [2–4], and applying engineered diffraction patterns for structural illumination [5–7]. These microscope designs provide not only two-dimensional sectioning, but also the ability to reconstruct 3-D fluorescence distribution within a specimen [8].

Recently, a new class of microscopy tools termed PALM (photoactivation localization microscopy), FPALM (fluorescent photoactivation localization microscopy), and STORM (stochastic optical reconsruction microscopy), inspired by single-particle tracking experiments, has been developed [9–16]. These techniques use the localization of individual photoswitchable fluorescent molecules to build up a representation of the underlying fluorescence distribution. Three-dimensional localization of single molecular images can be performed with 50–70 nm precision on axis and better laterally [13]. While these techniques yield reproducibly stunning results, the generation of systematic errors that are due to aberrations has not been investigated.

In most biological applications, the specimen is placed in an aqueous media with an index of refraction different from the mounting cover glass. Refraction at a glass–water interface causes an effective stretching of a 3-D image, an effect termed the focal shift [17]. The ratio between the actual height of a light source and its apparent separation from the interface depends mainly on the effective numerical aperture and the index of refraction difference, but

0003-6935/09/101886-05$15.00/0

not strongly on the depth of imaging and wavelength. It has been shown that the focal shift can be calculated [18] or measured experimentally [19,20] to correct 3-D images.

In addition to the focal shift, spherical aberrations are another major artifact caused by the index of refraction mismatch at the glass–water interface. The point spread function (PSF) is used to describe the composite blurring of a single point source by a microscope's imaging optics. As a result of spherical aberrations, the PSF is a changing function of a point source's depth in solution, termed the depth-varying (DV) PSF. It has been shown that the peak intensity of the PSF decreases with depth and that the PSF shape becomes asymmetric along the imaging axis [18,19,16,21]. We previously applied the DVPSF to 3-D deconvolution microscopy [21]. Similarly, the effect of spherical aberrations of sources at different depths needs to be taken into account when localizing single molecules during 3-D PALM or STORM imaging. We use experimentally measured PSFs at different imaging depths to show that, when the width of a defocused point source is used to determine a molecule's axial position, aberrations result in a nonuniformly compressed 3-D image. This effect is most significant at positions deeper than the image plane.

2. Methods

We used the DVPSF data from Shaevitz and Fletcher to examine the effect of spherical aberrations on axial particle localization [21]. Briefly, in that study a 170 nm green fluorescent bead was held at different depths in solution near a glass–water interface using an optical trap built on an inverted microscope capable of 3-D steering. An infinity-corrected apochromatic (Apo) total internal reflection fluorescence (TIRF) $100\times/1.49$ numerical aperture oil-immersion objective lens was used for trapping and imaging. We define a light source in the liquid to be above the water–glass interface. The depth of the focal plane and the trapped bead were controlled independently with a computer. The size of the bead is smaller than the diffraction limit but big enough to be reliably trapped with optical tweezers. Images of the fluorescent bead were recorded at different focal plane and bead depths relative to the cover glass position by use of a charge-coupled device (CCD) camera with a pixel size of 42 nm by 42 nm in the image plane. A more detailed description of the experimental setup was published previously [21]. All the depths and axial positions were corrected for the focal shift as described [21]. The full width at half-maximum (FWHM) of the image of a 200 nm fluorescent bead is 400 nm laterally and 600 nm axially.

All the analyses in this paper were performed by use of custom software written in Igor Pro (WaveMetrics, Portland, Oregon). The width for each lateral image within the DVPSF was found by fitting to a two-dimensional Gaussian function using a Levenberg–Marquardt algorithm to minimize the chi square:

$$I(x,y) = I_0 + Ae^{-\frac{x-x_0}{2\sigma^2}\frac{y-y_0}{2\sigma^2}}, \quad (1)$$

where I_0 is the background offset, A is the peak intensity, (x_0, y_0) is the lateral center of the peak, and σ is the lateral width of the peak. This method is valid when the axial displacement from the image plane is within a few wavelengths; images from larger displacements exhibit diffraction rings and are inappropriate for this type of analysis.

3. Results and Discussion

Shaevitz and Fletcher used an optical trap to systematically move a small fluorescent bead in the axial dimension relative to both the image plane and a glass–water interface [21]. Figure 1(a) displays images of a trapped bead 375 nm above, at, and below the image plane when the image plane was at the glass–water interface and 900, 1800, and 2700 nm in solution. Each lateral image was fit with a two-dimensional Gaussian function; see Eq. (1). Figure 1(b) shows the average bead image width σ as a function of two variables: the depth of the bead relative to the image plane (horizontal axis) and the depth of the bead relative to the water–glass interface (vertical axis). Figure 1(c) shows horizontal line scans through Fig. 1(b), the width as a function of the point source depth relative to the image plane, at five different image plane depths. Most notably, the width versus height function differs for a source in solution from that for a fixed point source on the glass–water interface [13]. This is consistent with previous observations that axial–medial sections through the PSF form a symmetric X shape in the absence of aberrations but are stretched along the axis in an asymmetric fashion at larger depths, resembling an inverted Y [18,22].

In practice, previous implementations of 3-D single-particle tracking used the measured change in image width with axial position for a surface-bound probe as a calibration data set. The data were then used to estimate the axial position of a measured probe in solution (see, e.g., Ref. [13]). The calibration data taken for a probe at the glass–liquid interface, however, does not account for aberrations that arise when imaging deeper in solution. The appropriate width-position data for this task (fixing the relative location of the image plane and the water–glass interface while changing the location of the bead) correspond to a line scan through Fig. 1(b) with a slope of one. Figure 2 shows a comparison of the width in the aberration-free case [the bottommost horizontal line scan through Fig. 1(b)] and the widths of the images of a bead with varying heights relative to the image plane with a fixed glass–water separation of 375 nm. The widths of the images of a defocused bead between the image plane and the interface do not deviate significantly from the aberration-free case (negative depth), whereas

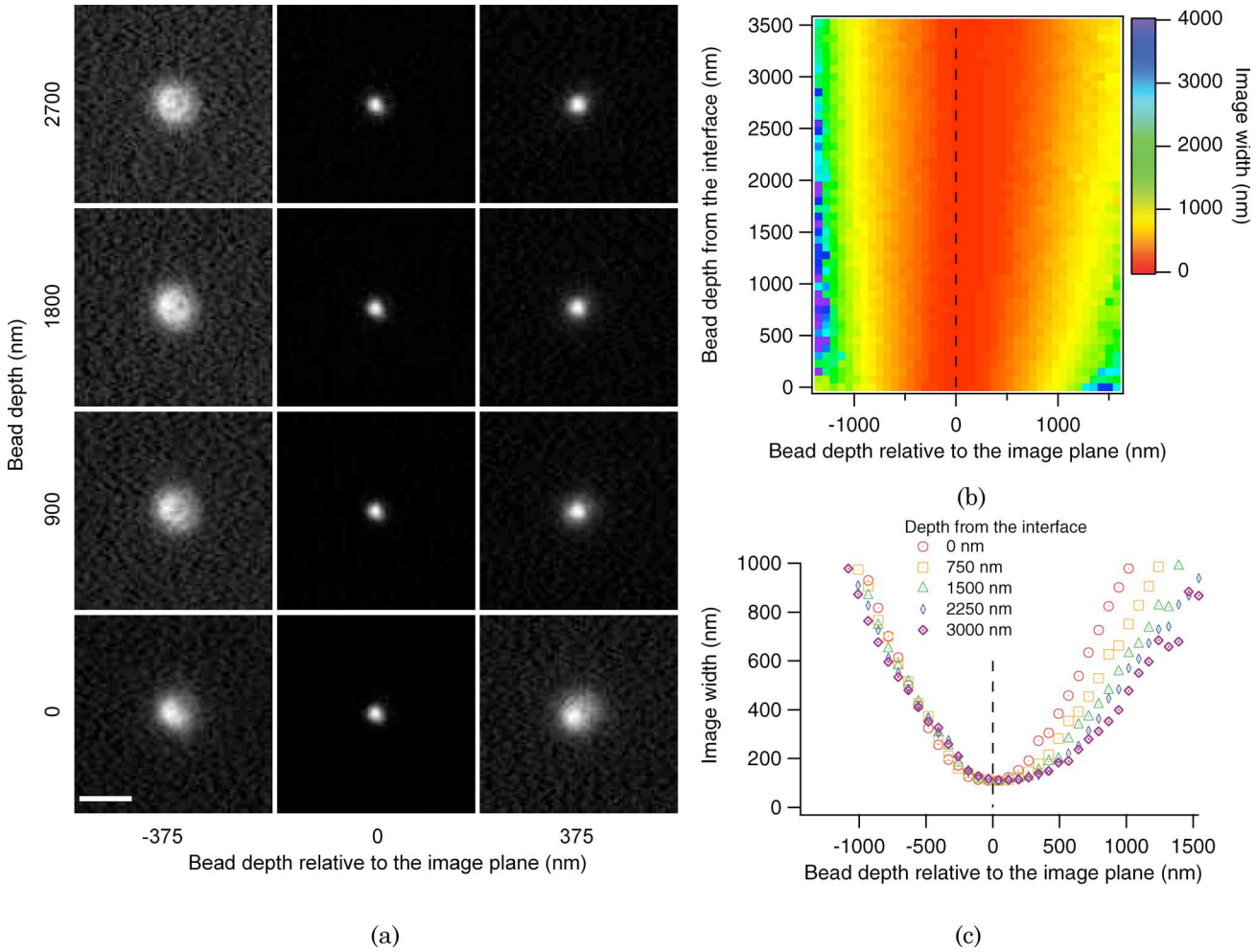

Fig. 1. (Color online) Typical in-focus and defocused images of a trapped fluorescent bead and the fit width of these images with a two-dimensional Gaussian function. (a) Images of the bead 375 nm below (column 1), on (column 2), and above (column 3) the image plane. The distance between the bead and the water–glass interface is chosen as 0 (aberration-free), 900, 1800, and 2700 nm. The scale bar is 1 μm. (b) The image width is plotted as a function of the distance of the bead from the glass–water interface and from the image plane. (c) Horizontal lines scans through (b) at imaging depths of 0, 750, 1500, 2250, and 3000 nm. The dashed line in (b) and (c) indicates the location of the image plane.

the bead above the image plane will appear smaller because of the asymmetrically stretched PSF (positive depth).

Use of the aberration-free PSF for calibration of a position estimation algorithm will lead to systematic errors. To calculate the magnitude of this error, we systematically estimated the depth of a bead image using both the aberration-free calibration curve and the DV calibration curve shown in Fig. 2. The estimated height was computed by a nearest-neighbor linear interpolation and then compared with the actual height. As an example, we fixed the distance between the image plane and the glass–water interface at 375 nm and calculated both the estimated position and the position error (Fig. 3). Because of the asymmetrically stretched PSF in solution, the calibration error also appears highly asymmetric about the image plane. In our particular example, the deviation is less than 30 nm when the source is below the image plane. In contrast, a source 675 nm above the image plane is estimated to be at position 502 nm. The systematic error monotonically increases as the distance between the point source and the water–glass interface increases. This error in height localization effectively creates a nonuniformly distorted image with compression above the image plane.

The shape of the PSF deep in solution depends strongly on the specific microscope setup. In water-immersion or air-immersion objective systems, the distance between two glass–water or glass–air interfaces determines the sign of the aberration. McNally *et al*. found that the shape of the axial–medial section of the PSF can form both an upright Y shape as in our study and an inverted Y depending on the thickness of the glass coverslip in their setup [22]. For oil-immersion objectives, the PSF is always an upright Y shape when the image plane is placed above the coverslip, resulting in a stretched scale and therefore a compressed image above the image plane. The magnitude of the aberrations also depends on the

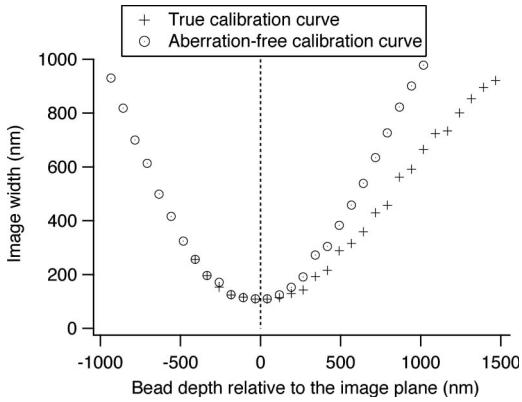

Fig. 2. Change in the width of a bead image with varying depth with (crosses) and without (circles) aberrations. The circles represent the widths of a source at varying depths relative to an image plane that is 375 nm above the glass–water interface. The vertical dotted line indicates the location of the image plane.

imaging depth, index of refraction of the mounting media, numerical aperture of the objective, and optical alignment. The variability in these parameters makes it difficult, in practice, to apply a universal correction to axial position calibration.

The images of the bead at different locations form Airy disks or more complicated forms in the presence of aberration. Far away from the focal point, the intensity of the higher-order diffraction rings in the PSF becomes significant. A Gaussian function is a good approximation only for the nearly in-focus images (the range scales with the vertical resolution of the objective), and we have analyzed data only in this range. Nonetheless, the width described by the simple Gaussian model already indicates the deviation between the real PSF from the aberration-free PSF. More physical models are required to quantify the deviation between the aberration-free PSF and the true PSF at larger distances. The original data were obtained from the optical trapping experiments. It is known that the scattering force produced by an optical trap tends to shift a trapped object from the exact focal point, and therefore the change in shape of the PSF that is due to aberration can contribute to the variable distance between the bead and the object plane. However, this effect was proved to be small by experimental data. In Neuman *et al.*, where the position of the bead was physically measured by the diffraction pattern of the bead and the interface, this shift was shown to be a constant [20]. In addition, at one particular collimation of the trapping laser, the minimum width of the bead image was achieved regardless of the magnitude of aberration. This suggests that the actual location of the bead is not far from the image plane compared with the systematic error caused by the calibration method without the consideration of aberrations.

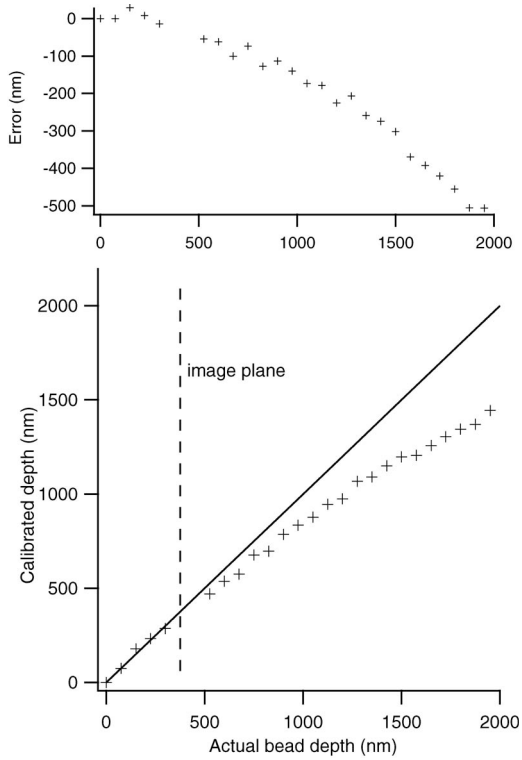

Fig. 3. Apparent height of a bead calibrated with the zero-depth, aberration-free, PSF as a function of the actual depth. The glass–water interface was placed 375 nm below the image plane. A straight line of slope 1 (solid line) is drawn as a guide to the eye. The vertical dashed line indicates the location of the image plane. The top figure shows the absolute localization error.

4. Conclusion

The index of refraction mismatch at a glass–water interface causes imaging artifacts in 3-D microscopy including the focal shift and an axial stretching that is due to spherical aberrations. An experimentally determined depth-varying PSF exhibits an asymmetric shape deep in solution because of spherical aberrations. Using an oil-immersion objective, the PSF changes from a symmetric X shape without aberrations to an asymmetrically stretched Y shape when the point source is above the image plane in solution. If the width–depth relation is used as a calibration method to measure the axial position of a single fluorescent particle, e.g., in superresolution localization-based microscopy techniques, aberrations become essential and should be considered separately in addition to the focal shift. Since the depth-varying PSF is stretched only above the image plane, the distortion of the height calibration is also nonuniform. When the aberration-free PSF is used for height calibration, the resulting localization results are compressed above the image plane by ~30%, whereas below the image plane, the relative systematic error is less than 10%.

Optical tweezers can be used to measure the DVPSF and thereafter reliably calibrate the image width–height relation. For oil-immersion objectives, if the measurement of the PSF in solution is not available, placing the image plane deep in the solution and using only the height calibration between the image plane and the water–glass interface will

produce satisfactory results. For water-immersion objectives, spherical aberrations can be minimized by properly setting the correction collar, which would virtually eliminate the calibration error.

This research was supported by National Institutes of Health (NIH) grant P50GM07150 and the Alfred P. Sloan Foundation.

References

1. J. G. White, W. B. Amos, and M. Fordham, "An evaluation of confocal versus conventional imaging of biological structures by fluorescence light microscopy," J. Cell Biol. **105**, 41–48 (1987).
2. W. Denk, J. H. Strickler, and W. W. Webb, "Two-photon laser scanning fluorescence microscopy," Science **248**, 73–76 (1990).
3. S. W. Hell and J. Wichmann, "Breaking the diffraction resolution limit by stimulated-emission: stimulated-emission-depletion fluorescence microscopy," Opt. Lett. **19**, 780–782 (1994).
4. R. Schmidt, C. A. Wurm, S. Jakobs, J. Engelhardt, A. Egner, and S. W. Hell, "Spherical nanosized focal spot unravels the interior of cells," Nat. Methods **5**, 539–544 (2008).
5. S. W. Hell and E. Stelzer, "Properties of a 4Pi confocal fluorescence microscope," J. Opt. Soc. Am. A **9**, 2159–2166 (1992).
6. M. G. Gustafsson, D. A. Agard, and J. W. Sedat, "1^5 m : 3D widefield light microscopy with better than 100 nm axial resolution," J. Microsc. **195**, 10–16 (1999).
7. M. G. L. Gustafsson, "Nonlinear structured-illumination microscopy: wide-field fluorescence imaging with theoretically unlimited resolution," Proc. Natl. Acad. Sci. USA **102**, 13081–13086 (2005).
8. J. W. Shaevitz, "Super-resolution for a 3D world," Nat. Methods **5**, 471–472 (2008).
9. S. T. Hess, T. P. K. Girirajan, and M. D. Mason, "Ultra-high resolution imaging by fluorescence photoactivation localization microscopy," Biophys. J. **91**, 4258–4272 (2006).
10. E. Betzig, G. H. Patterson, R. Sougrat, O. W. Lindwasser, S. Olenych, J. S. Bonifacino, M. W. Davidson, J. Lippincott-Schwartz, and H. F. Hess, "Imaging intracellular fluorescent proteins at nanometer resolution," Science **313**, 1642–1645 (2006).
11. M. J. Rust, M. Bates, and X. Zhuang, "Sub-diffraction-limit imaging by stochastic optical reconstruction microscopy (STORM)," Nat. Methods **3**, 793–795 (2006).
12. M. F. Juette, T. J. Gould, M. D. Lessard, M. J. Mlodzianoski, B. S. Nagpure, B. T. Bennett, S. T. Hess, and J. Bewersdorf, "Three-dimensional sub-100 nm resolution fluorescence microscopy of thick samples," Nat. Methods **5**, 527–529 (2008).
13. B. Huang, W. Wang, M. Bates, and X. Zhuang, "Three-dimensional super-resolution imaging by stochastic optical reconstruction microscopy," Science **319**, 810–813 (2008).
14. H. P. Kao and A. S. Verkman, "Tracking of single fluorescent particles in three dimensions: use of cylindrical optics to encode particle position," Biophys. J. **67**, 1291–1300 (1994).
15. A. Yildiz, J. N. Forkey, S. A. McKinney, T. Ha, Y. E. Goldman, and P. R. Selvin, "Myosin V walks hand-over-hand: single fluorophore imaging with 1.5 nm localization," Science **300**, 2061–2065 (2003).
16. F. Aguet, D. Van De Ville, and M. Unser, "A maximum-likelihood formalism for sub-resolution axial localization of fluorescent nanoparticles," Opt. Express **13**, 10503–10522 (2005).
17. J. Bewersdorf, A. Egner, and S. W. Hell, "Multifocal multiphoton microscopy" in *Handbook of Biological Confocal Microscopy*, J. B. Pawley, ed., 3rd ed. (Springer, 2006), Chap. 29.
18. C. J. R. Sheppard and P. Torok, "Effects of specimen refractive index on confocal imaging," J. Microsc. **185**, 366–374 (1997).
19. A. Diaspro, F. Federici, and M. Robello, "Influence of refractive-index mismatch in high-resolution three-dimensional confocal microscopy," Appl. Opt. **41**, 685–690 (2002).
20. K. C. Neuman, E. A. Abbondanzieri, and S. M. Block, "Measurement of the effective focal shift in an optical trap," Opt. Lett. **30**, 1318–1320 (2005).
21. J. W. Shaevitz and D. A. Fletcher, "Enhanced three-dimensional deconvolution microscopy using a measured depth-varying point-spread function," J. Opt. Soc. Am. A **24**, 2622–2627 (2007).
22. J. G. McNally, C. Preza, J. A. Conchello, and L. J. Thomas, "Artifacts in computational optical-sectioning microscopy," J. Opt. Soc. Am. A **11**, 1056–1067 (1994).